Monitoring freshwater–saltwater interfaces with SAMOS – installation effects on data and inversion

Mathias Ronczka*, Thomas Günther, Michael Grinat and Helga Wiederhold

Leibniz Institute for Applied Geophysics, Hannover, Germany

ABSTRACT

A major problem for the freshwater supply of coastal regions is the intrusion of saltwater into aquifers. Due to extensive extraction of freshwater to suffice increasing drinking water demands and/or in periods of reduced groundwater recharge, the equilibrium state may be disturbed. The result is an upconing or movement of the fresh–saline groundwater interface, which reduces the local drinking water resources at coastal regions or islands. The saltwater monitoring system (SAMOS) is a vertical electrode chain installed in a backfilled borehole. It provides a solution to observe the transition zone in detail, both temporally and spatially. We present monitoring data of the first year from three locations - with different geological conditions that show disturbances in the resistivity distribution that result from the drilling processes. A clayey backfilling, for example, can lead to beam-like artefacts, and a mixed fluid within the backfilling changes its bulk resistivity, both leading to misinterpretations. We performed data inversion under cylindrically symmetrical conditions in full-space in order to separate these resistivity artefacts from the undisturbed background. Data inversion reveals that it is possible to separate drilling effects on the resistivity distribution from the undisturbed background. Thus, an interpretation of the natural transition zones can be made immediately after the installation.

Key words: Electrical resistivity tomography, Groundwater, Hydrogeophysics.

INTRODUCTION

Usually, seawater and freshwater are in an equilibrium state in coastal regions, forming the well-known saltwater wedge. In case of a homogeneous subsurface, it takes the form of a concave plane towards inland, replacing freshwater due to its higher density. However, increasing population, human overexploitation and climate change put pressure on coastal regions.

The demographic change leads to faster growing cities in the coastal regions. That leads to an extensive extraction of freshwater to suffice increasing drinking water demands. Periods of reduced groundwater recharge may disturb the equilibrium state of the freshwater-saltwater interface. The result is saltwater upconing or a movement of the fresh-saline interface, which reduces local drinking water resources at coastal regions or islands.

Several earlier hydrogeological investigations study, for example, the pumping optimization or the impact of climate change on seawater intrusion in coastal aquifers (e.g. Rasmussen *et al.*, 2013; Ferguson and Gleeson, 2012; Sherif *et al.*, 2012; Cheng *et al.*, 2000; Wiederhold *et al.*, 2013), and support the local water supply companies (e.g. Schöniger *et al.*, 2019).

For geophysical investigations of the subsurface for hydrological purposes, electrical/electromagnetic methods are often chosen because the electrical resistivity is an indicator for both clay content and groundwater salinity. The spectrum of methods extends from electrical resistivity tomography (ERT) to electromagnetic methods in time and frequency domain. Electrical resistivity is commonly mapped in two- or three-dimensional applications, as summarized in

*E-mail: m.ronczka@gmail.com

Loke *et al.* (2013). In particular, the ERT monitoring of resistivity changes is capable of imaging transport processes in the subsurface (Kemna *et al.*, 2002). In recent years, more permanently installed ERT systems have been presented that monitor groundwater flow between surface water and groundwater (Coscia *et al.*, 2011), in landslides (e.g. Whiteley *et al.*, 2019 and the references therein), or in karst systems (Watlet *et al.*, 2018). According to the measurement speed and the model resolution properties, another typical application is the characterization and monitoring of freshwater aquifers that suffer from saltwater intrusion. A recent investigation addresses the development of automated monitoring systems like the ALERT (automated time-lapse electrical resistivity tomography) system (Kuras *et al.*, 2009; Ogilvy *et al.*, 2009). Binley *et al.* (2002) observed variations in moisture content with different methods, including single borehole ERT, and could resolve changes between 0.5 and 1%. Tsourlos *et al.* (2003, 2007) presented the concept of single borehole ERT monitoring including data inversion by assuming point electrodes. They found that this approach provides subsurface images of increased resolution compared to surface-based geophysical methods.

To analyse particular structures, for example the interface between saltwater-bearing and freshwater-bearing sediments, it is best to install the electrode array in the immediate proximity of these structures. Grinat *et al.* (2010) briefly described our self-developed measuring system SAMOS (Saltwater Monitoring System) that combines several advantages:

- the electrode array is installed in the subsurface covering the whole transition zone between freshwater and saltwater,
- it is a low-power system and it can be buffered by solar power,
- the measurements are carried out automatically several times a day, and
- data are regularly transferred by telemetry.

SAMOS was, aside from ALERT, one of the first self-sustaining monitoring systems when it was installed first in 2009. It was designed as a low-power system with a rechargeable power supply (by solar panel) and automatic data transfer. Recently, a commercial monitoring system has become available, which includes data handling (Baisset and Neyens, 2018). In this paper, we present the monitoring data and the time-lapse inversion results from three cases:

- an undisturbed ideal test site with simple geologic conditions,
- a more geologically complex site in the vicinity of the previous test site, and

- a new test site where measurements were recorded directly after the installation and there were severe effects on the collected data caused by disturbed conditions due to the the drilling process.

All existing publications on such tools assume point electrodes. However, for small electrode distances compared to the dimensions of the borehole tool, the electrodes cannot be considered points in the full space anymore. Rücker and Günther (2011) used the so-called complete electrode model (CEM) to account for the real shape of the ring electrodes for injecting the current and measuring the voltage. They already modelled a very similar borehole tool using the exact geometry and found significant differences, particularly for short electrode arrays. Such systematic errors would lead to inversion artefacts near the borehole. A simple correction of geometrical factors could help, but is not guaranteed to be sufficient as shown by Doetsch *et al.* (2010) for crosshole ERT.

Therefore, we present an inversion approach that takes the 3D geometry of the borehole and the electrodes into account by using the CEM technique; full 3D forward modelling has been performed. For inversion, we reduce the dimensionality to 2D assuming a cylindrical symmetry, and, therefore, we could discretize the near-borehole and the far-borehole regions. The main objective of this article is to find out if the disturbance of the resistivity distribution, caused by the drilling process, can be separated from the undisturbed background resistivity through inversion. After introducing the three test sites and the SAMOS system in detail, we describe the numerical data analysis that inverts the data into 2D subsurface images, thus differentiating between the near-borehole and the undisturbed areas, for different time steps. We discuss the data base and the static inversion results along with the lithology obtained from the boreholes. Finally, we present the dynamic behaviour for several months since installation, and interpret these results in terms of processes in the disturbed and undisturbed zones.

MONITORING SYSTEMS AND SITES

Two readily developed and self-built monitoring systems were installed at the North Sea island Borkum in the project CLIWAT (climate and water) in September 2009. Monitoring data had been collected since then with only little gaps due to technical problems.

The third system was manufactured by SolExperts for the project goCAM (go coastal aquifer management). It was installed in 2018 near the village Abickhafe at the Ems-Jade canal, approximately 10 km west from its estuary next to a
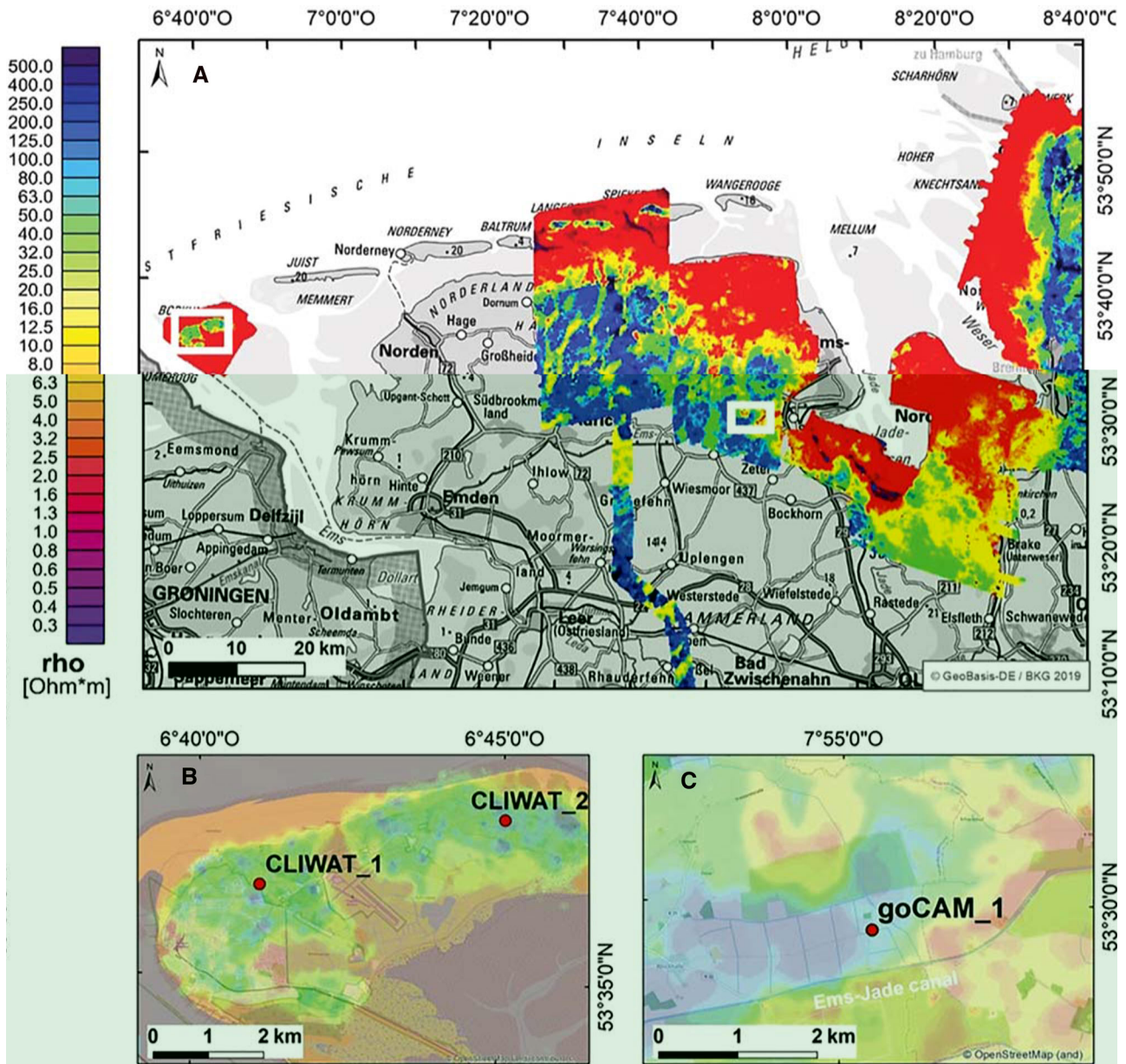
Figure 1 (a) Location map with a slice in 15 depth showing electrical resistivities derived from HEM results (Siemon *et al.*, 2018); (b) detailed monitoring position of CLIWAT1 and CLIWAT2 in Borkum; and (c) at Abickhafe (goCAM1) near the Ems-Jade canal. White frames in (a) show the location of cut-outs in (b) and (c).

chloride-monitoring site. Figure 1 shows the location of the monitoring systems and the resistivity slices in 15 m depth derived from airborne electromagnetic investigations (HEM).

Low resistivities (red) indicate mostly saltwater in the open sea and coastal saltwater intrusion that reaches several kilometres inland, but occasionally also clay deposits (Siemon *et al.*, 2015). On the mainland, the freshwater–saltwater interface forms a front roughly parallel to the coast. Its shape is

mainly influenced by geologic conditions and early age flooding events. Borehole logs at goCAM1 show mostly Quaternary sand deposits with embedded clay lenses (see Fig. 2).

Figure 3 shows data of installed chloride monitoring next to goCAM1, at two different depths. The concentrations at 30 m depth are almost constant at ≤20 mg/l and at ≈450 mg/l in 55 m depth with a slight increasing trend. Although the values exceed the 250 mg/l threshold for drinking water, no
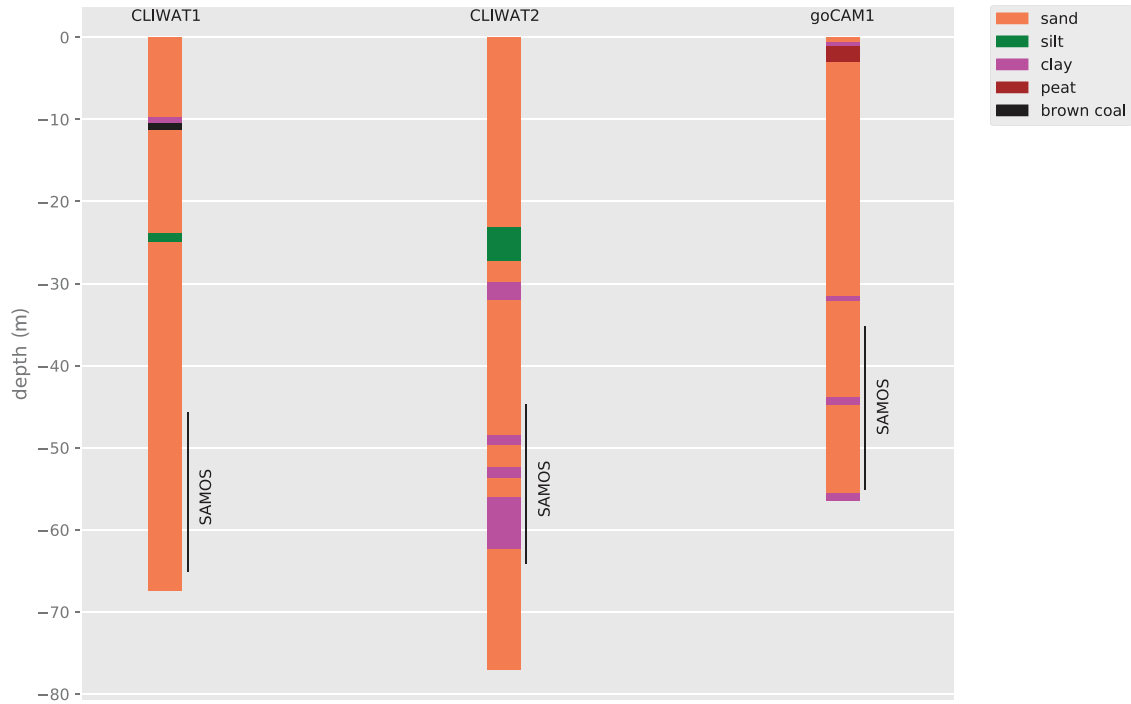
Figure 2 Lithologic logs for the monitoring sites at the island Borkum (CLIWAT1, CLIWAT2) and the village Abickhafe (goCAM1), including the depth level of the monitoring system SAMOS.

information about the transition zone is given. At this point, the SAMOS monitoring system becomes important, as it delivers data along a vertical profile in a defined depth range and is able to image the transition zone form fresh to saline water.

According to Schneider and Kruse (2006), the freshwater lens on islands is controlled by several factors like recharge rate, stratigraphy, elevation, vegetation and tidal effects. The Ghyben–Herzberg (GH) relation states that the saltwater
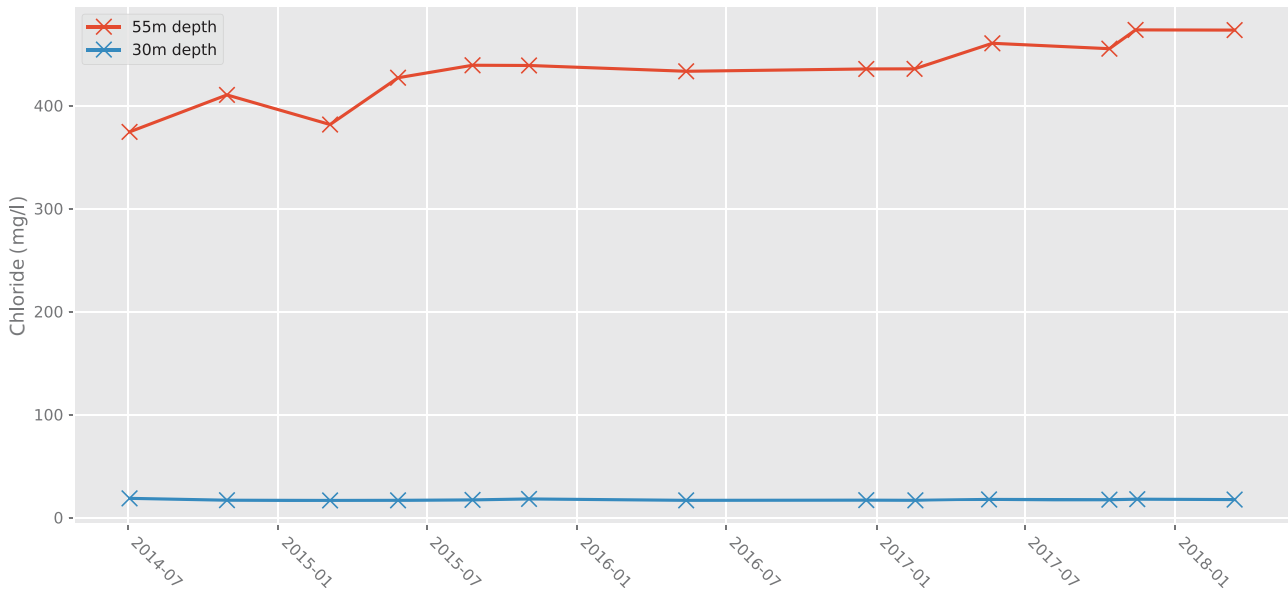

Figure 3 Chloride concentrations at goCAM1 derived from fluid conductivity measurements of a monitoring in 30 m (blue) and 55 m (red) depth.
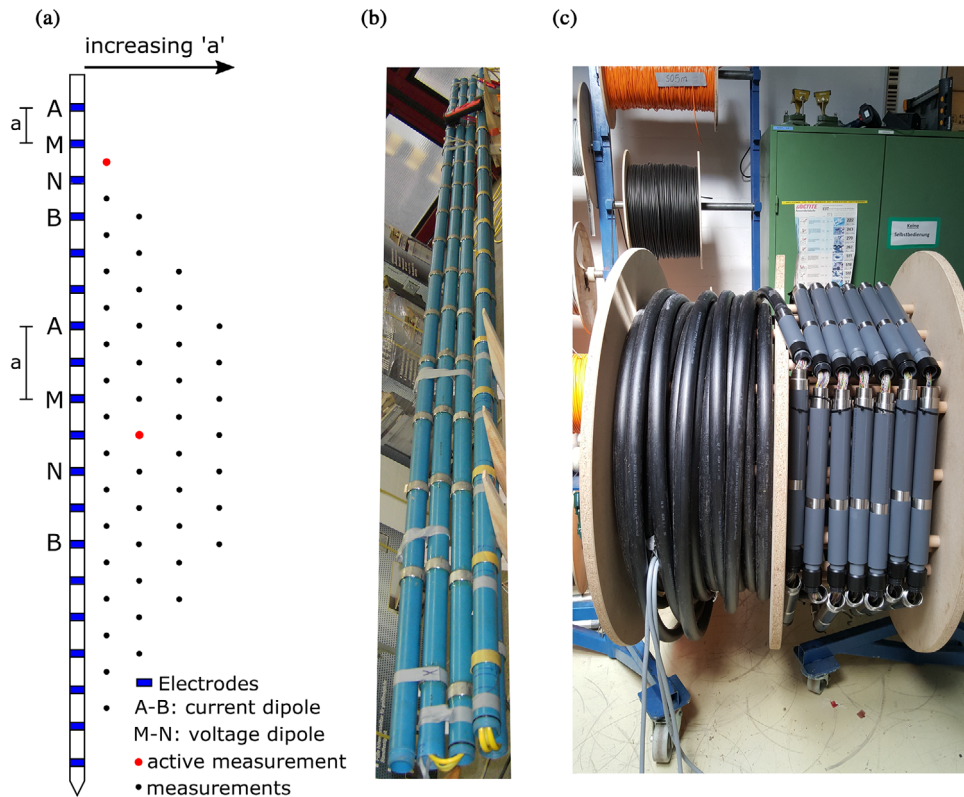
Figure 4 Schematic sketch of the SAMOS geoelectrical measurement system (a), the CLIWAT chains installed in Borkum (b), and the goCAM1 system (c).

interface depth is directly proportional to the elevation of the groundwater table above the sea level. Assuming a typical saltwater density of $\rho_s = 1.025$ g/cm^3 for the North Sea, we obtain an approximation for the depth of the saltwater/freshwater interface of $h_{bsl} \approx 40*h_{asl}$, with h_{asl} being the elevation of the groundwater table above the sea level. However, the thickness of the freshwater lens also depends on the ratio between recharge rate and hydraulic conductivity, and the size of the island. The thickness of the transition zone between freshwater and saltwater, which is not included in the GH model, is mainly influenced by the tidal range and aquifer parameters (Cooper, 1959).

The general geological condition at Borkum shows Holocene sandy sediments deposited as an alluvial formation, which consists of silica sand with lenses and enclosures of peat, clay, silt and shell detritus (Igel *et al.*, 2013). Lithological information of the CLIWAT1 borehole in Fig. 2 shows mostly fine-grained sand down to 70 m depth, which is interrupted by a thin clay and brown coal layer at 10 m depth. Compared to the homogeneous conditions at the first location, CLIWAT2 shows a more complex pattern. The bottom of the first fine grained sand layer is at 23.10 m depth,
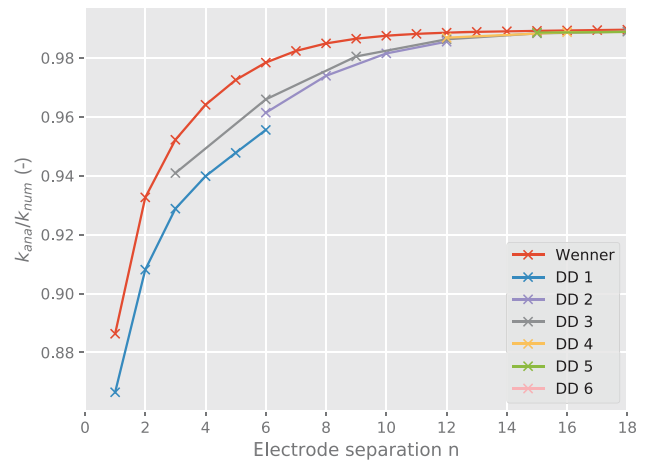

Figure 5 Ratio between numerical and analytical geometrical factors for Wenner-α and dipole–dipole array. Point electrodes were assumed for k_{ana} and CEM electrodes for k_{num}. DD1–DD6 describe different dipole lengths.

followed by a 4.20 m thick silt formation. The third layer from 27.3 to 35 m depth consists of medium-grained sand and is interrupted by a clay formation at 29.9–32 m depth range. The following fine-grained sand ends at 48.5 m depth.
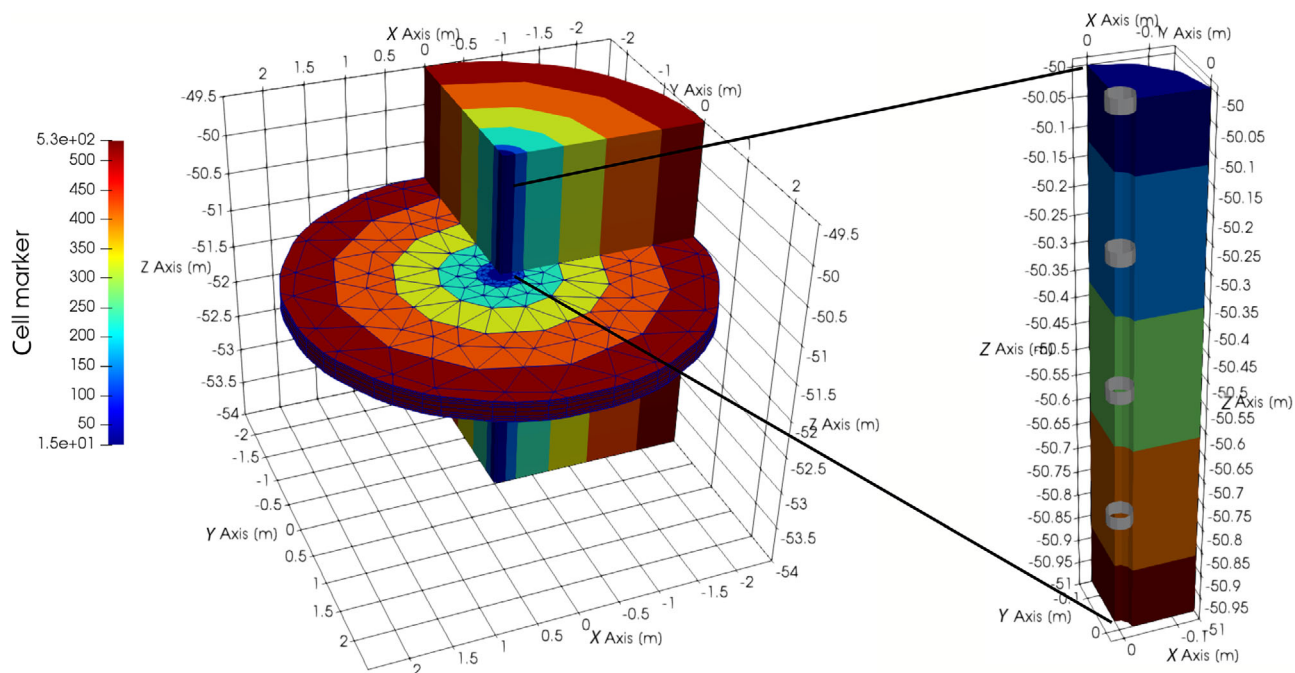
Figure 6 Cylindrically symmetric FE mesh, with a horizontal slice showing the cell marker distribution (left). The right side shows an enlarged version of the inner cylindrical segment and its vertical marker distribution including facets representing ring electrodes (grey).

Ground-penetrating radar investigations have been done to estimate the freshwater lens by locating the water table (Igel *et al.*, 2013). Additionally, numerical groundwater modelling has also been carried out by Sulzbacher *et al.* (2012) to study the freshwater lens and to use it as a basis for further simulations. They used 124 water-sample analyses from sea water at different locations, from water supply wells, new drillings or direct push measurements. They derived a constant temperature-dependent factor to transfer electrical conductivity values into total desolved solids (TDS). From the resulting TDS distribution at the surface, a constant-mass boundary condition was constructed. The freshwater lens of the island is modelled including different historical water-relevant events. The computed TDS distribution for the year 2008 is then compared with the electrical conductivities from HEM data.

Both SAMOS boreholes in Borkum were drilled by a hydraulic rotary drilling/directional drilling, which interacted with the borehole vicinity, changing its electrical properties due to the used mud. The final installation depth for CLIWAT1 was at 45.75–66 m and for CLIWAT2 from 44.75 to 65 m. In contrast, air drilling was used for goCAM1, resulting in a much smaller disturbed zone near the borehole. The installation depth was shallower compared to CLIWAT, being in the range of 35.25–55 m.

Standard hydrological approaches for monitoring saltwater intrusions are, for example, fluid conductivity measurements within boreholes at specific depths or multilevel sampling which has the difficulty of circulating the fluid in the borehole. In comparison, SAMOS can image the electrical resistivity changes based on the water conductivity along a vertical profile.

The installed electrode chains in Borkum consist of a PVC casing DN35 with a diameter $d = 48$ mm and 78 stainless steal ring electrodes with a height of 25 mm and a spacing of 0.25 m in-between. The goCAM system consists of 80 stainless steel (1.4435) ring electrodes with the same height and spacing, but a diameter of 50 mm. The only main difference between the CLIWAT and goCAM monitoring systems is in the length of non-flexible parts. Figure 4 shows that CLIWAT1 and CLIWAT2 systems consisting of four 5–6 m long parts, while the goCAM1 system was build of smaller (0.5 m long) parts to ease the installation. The wiring of all systems occurs inside the PVC tube, which makes the system robust against mechanical stress during installation. Two O-ring seals on the screw fitting make the contact between segments water-tight. Decoder boxes connect the electrodes with the '4point light 10W' instrument manufactured by LGM, which is used to perform the measurements. It is a low-power device with an output current of 1 μA–100 μA and voltage of 380 V. The power supply is

Table 1 Data range with minimum and maximum apparent resistivities, number of iteration, and the rrms error for the base-line inversion of all three test sites. The last two columns give the iteration- and relative root mean square (rrms)-range for the shown time-lapse results

Site	Base line			Time lapse	
	Data (min/max)(Ωm)	Iterations	rrms (%)	Iteration range	rrms range (%)
CLIWAT1	1.75/89.68	2	1.9	1–4	1–9
CLIWAT2	2.35/83.69	3	6.7	3	5–10
goCAM1	12.46/242	5	1.9	3–5	1.9–2.2

ensured by batteries connected to a solar panel. An additional solar panel completes the surface installation to recharge the battery used for power supply. The system is designed to run automatically, starting a predefined protocol file that contains electrode configurations at a desired time. Data are uploaded daily to an ftp server.

The schematic sketch in Fig. 4(a) shows the principle of measurement with the SAMOS system, and how the so-called pseudosection is constructed for a Wenner-α array. The go-CAM1 system was installed in December 2018 and runs with a Wenner-α and dipole–dipole array that records 3167 data points for one time step. Both datasets have been combined to

get a better coverage and resolution. The monitoring at CLI-WAT1 and CLIWAT2 in Borkum started in 2009, measuring a Wenner-α configuration with about 900 data points per time step and five steps a day.

NUMERICAL MODELLING

We used the Python-based open-source software package py-GIMLi (Rücker *et al.*, 2017) for data handling, forward modelling and inversion. For analysing the data with respect to structures and changes in the subsurface, the correct geometry of the SAMOS installation needs to be taken into account.
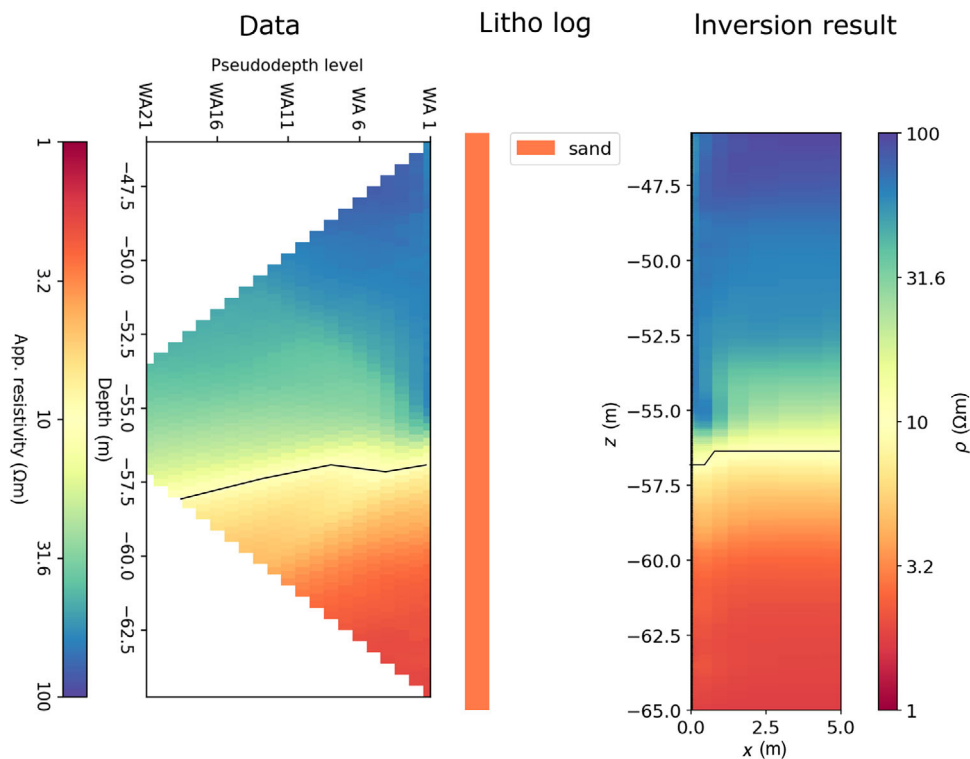

Figure 7 Pseudosection of the base-line measurements from CLIWAT1, together with the lithological log (middle) and the inversion result (right). The black line marks the 10 Ωm interface.
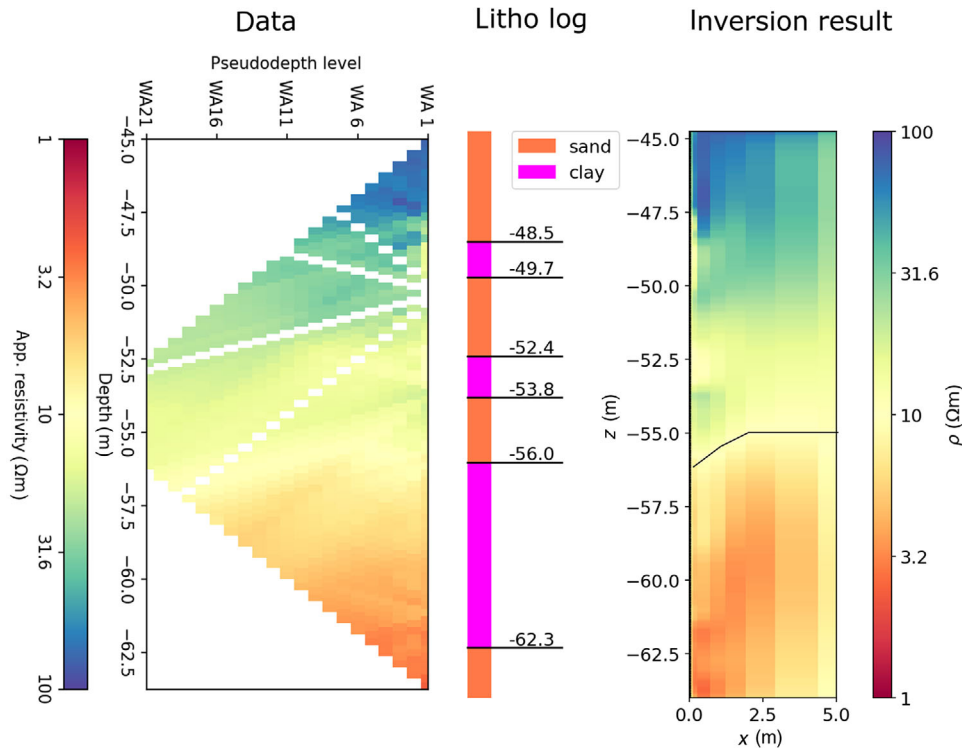
Figure 8 Pseudosection of the base-line measurements from CLIWAT2, together with the lithological log (middle) and the inversion result (right).

The two major components are the central plastic tube, which acts as an insulator and the ring electrodes. We used TetGen (Si, 2015) to create tetrahedral meshes that discretize the plastic tube as a void with Neumann boundary conditions and the ring electrodes approximated by polygon faces with their specific height and diameter.

The ring electrodes cannot be treated as points because of their extension compared to their distance, which leads to a three-dimensional (3D) modelling problem. We used the complete electrode model (CEM), which allows the current injection and voltage measurement over the whole surface using a (in this case small) shunt impedance (Rücker and Günther, 2011). Ronczka *et al.* (2015) compared CEM with other approaches for modelling extensive electrodes like the conductive cell model (Rucker *et al.*, 2010), and concluded that CEM is widely equivalent, but more flexible and efficient. We calculated the analytical geometrical factors (assuming point electrodes) for a Wenner-α using $k_W = 4\pi a$ and dipole–dipole array by $k_{DD} = 2\pi n(n + 1)(n + 2)a$, with a being the electrode spacing and n the factor for the spacing between the current and the potential electrodes. Note that the analytic k-factor does not take the PVC tube of the monitoring system nor the electrode shape into account. We also calculated numeri-

cally the geometric factors (k_{num}) by assuming a homogeneous full-space of 1 Ωm and modelling the electrodes with CEM. Figure 5 shows that maximum deviation of 11.4% for Wenner-α and 13.4% for dipole–dipole occuring for the smallest electrode separations and it decreases to approximately 1% for both array types. Therefore, it is most important to consider the correct electrode geometry for small electrode separations.

As full pseudosections are measured, we are able to image the resistivity distribution in two dimensions as a function of depth and distance to the borehole. This is because although the forward problem is essentially three-dimensional because of the considered electrode geometry, the information content is two dimensional. We solved this issue by using a hybrid scheme allowing a 3D forward calculation with a reduction of the model to two dimensions for the inversion. To this end, we created a triangular prism-mesh based on a number of 10 rings representing different distances to the borehole. All cells at the same depth and distance are associated with the same cell marker, creating a multi-cell region. All regions are treated as so-called single regions, which are represented by only one unknown (resistivity) during the inversion, while for the forward computation the cylindrially symmetrical 3D resistivity
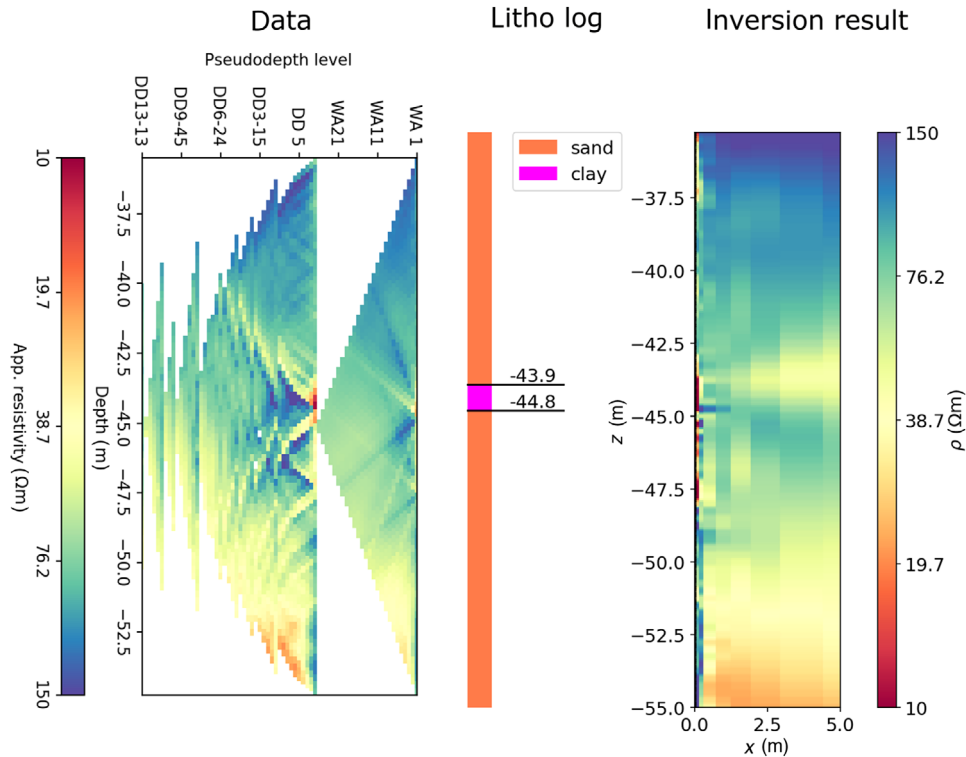
Figure 9 Pseudosections for Wenner-α (WA) and dipole–dipole (DD) array of the baseline measurement from goCAM1, along with the corresponding lithological log (middle) and the inversion result (right).

is used. This is known as the region technique in pyGIMLi (e.g. Coscia *et al.*, 2011).

Although this approach strongly constraints the information content, one can retrieve it is reasonably, as it is obviously not possible to resolve 3D resistivity distributions using a 2D electrode setup.

Figure 6 illustrates the cell marker distribution in the finite element (FE) mesh, with a horizontal slice showing circular segments with their constant cell markers. The inner cylinder segment in Fig. 6 (right) shows the vertical marker distribution together with grey facets representing the ring electrodes. The hollow cylinder in the centre of the FE mesh represents the PVC-cased electrode chain.

Between the individual regions, smoothness constraints are used and the regularization parameter is chosen so that the smoothest model that fits the data within a given error is considered to be final. We assume a constant relative error of 3%, because we do not expect a voltage dependency due to the small distances and the good coupling. A reference-model-based approach for the time-lapse inversion was chosen with the first model as a base-line; a smooth distribution (relative to the logarithmic model transformation) of the resistivity changes is targeted. We did not use a difference inversion

scheme, which removes systematic misfits by subtracting the base-line data, because this could partially remove the near-borehole effects that we want to capture.

All subsequent inversion results are plotted as 2D images that are functions of borehole distance and depth. We performed smoothness-constrained time-lapse inversions for all test sites to find out if the drilling-induced resistivity variations in the borehole vicinity could be mitigated in order to restore the undisturbed background resistivity distribution.

RESULTS

Static inversion

The overall data quality in all three test sites is very good with the stacking errors less than 1%. However, the electronic parts at the surface installation were affected by an increased moisture content that led to outliers following the pattern of a defect electrode. A basic data processing removed these errors prior to the inversion. The data fit for all base-line inversions is given in Table 1.

The base-line results in Fig. 7 for CLIWAT1 show apparent resistivity in the range of 2–80 Ωm and a transition
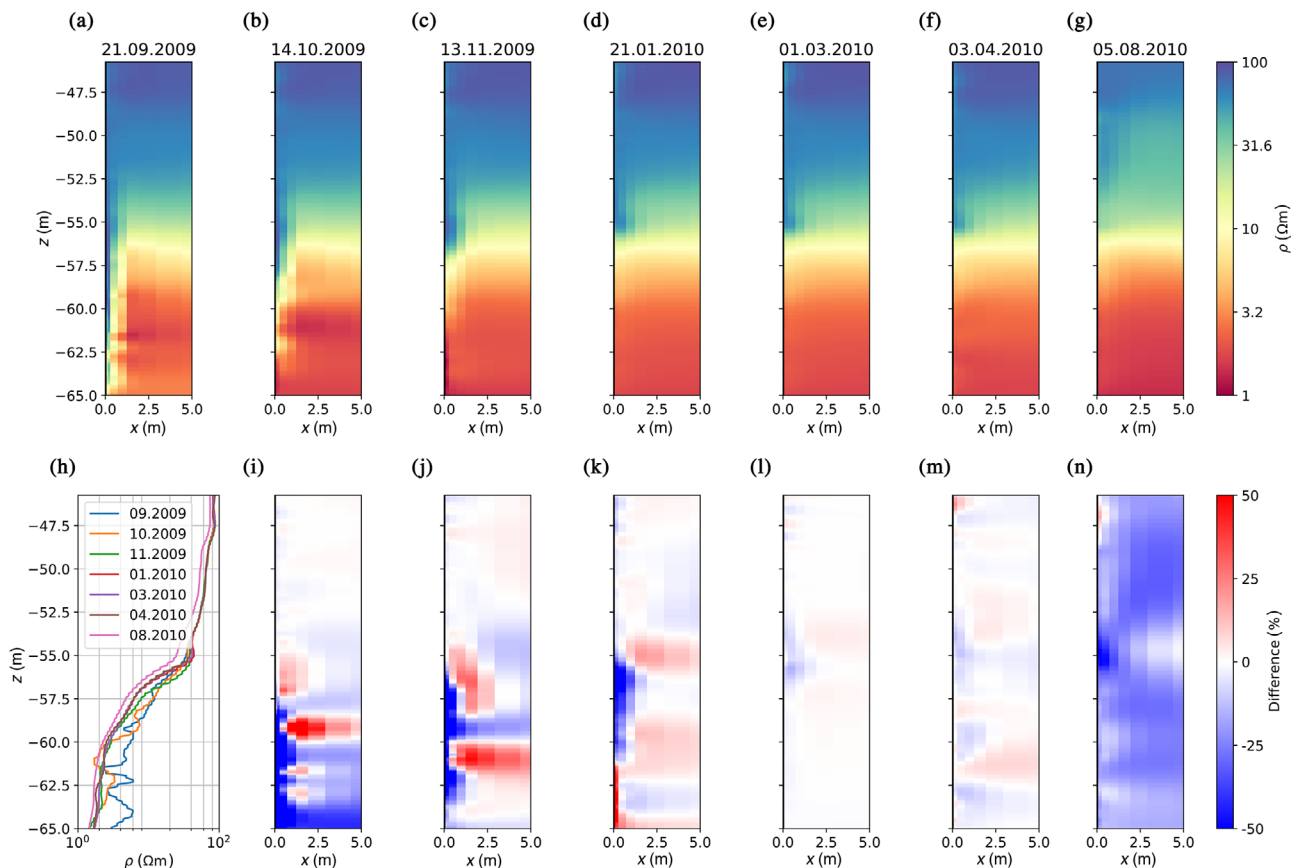
Figure 10 Dynamic inversion results from CLIWAT1, showing absolute resistivities (top) and relative differences towards the previous time step. Resistivities at 1 m distance from the electrode chain are shown in (h) for all time steps.

to lower values at approximately 56.5 m depth. The transition zone appears relatively thin for data with short electrode spacings, but smears out at larger separations. Regarding the simple local geological conditions (only sandy material), given by the lithology log, it can clearly be attributed to the interface between fresh and saline water. The inversion result on the right-hand side of Fig. 7 reproduces the transition zone at a similar depth (denoted by the black 10 Ωm line) with a slight variation for $x \leq 1$ m. The resistivity that follows is strictly layered for distances greater than 1 m, from which we conclude that there is no influence from the drilling process. However, model parts adjacent to the electrode chain are significantly different from the background, particularly in the depth range between 53 and 56 m. We interpret these higher resistivities as remains of the drilling process. The backfilling material is filled in without compaction resulting in a subsidence process that reduces the porosity with time. As long as this process continues, the porosity of the backfilled region

is higher compared to the background, which leads to a decreased resistivity. The whole transition zone is rather wide and extends from 47 m (with 100 Ωm) down to 60 m (with 2 Ωm). Note that this is not an effect of the smoothness in the inversion, but is real, as already shown by borehole measurements (e.g. Günther and Müller-Petke, 2012).

As shown in Fig. 8, the apparent resistivities for the baseline of CLIWAT2 range between 2 and 83 Ωm, comparable to CLIWAT1. However, the Wenner-α pseudosection on the left side of Fig. 8 is more structured, showing resistivity variations especially in the first few pseudo-levels. This is most likely caused by the more complex local geological condition compared to CLIWAT1. Three clay lenses at depth intervals of 48.5–49.7 m, 52.4–52.8 m, and 56–62.3 m appear in the lithological log. The upper two cause decreased resistivities for small separations, which are also different from the larger ones at the same positions, thus indicating strong influence from the drilling. It becomes clear that both the pseudosection and the
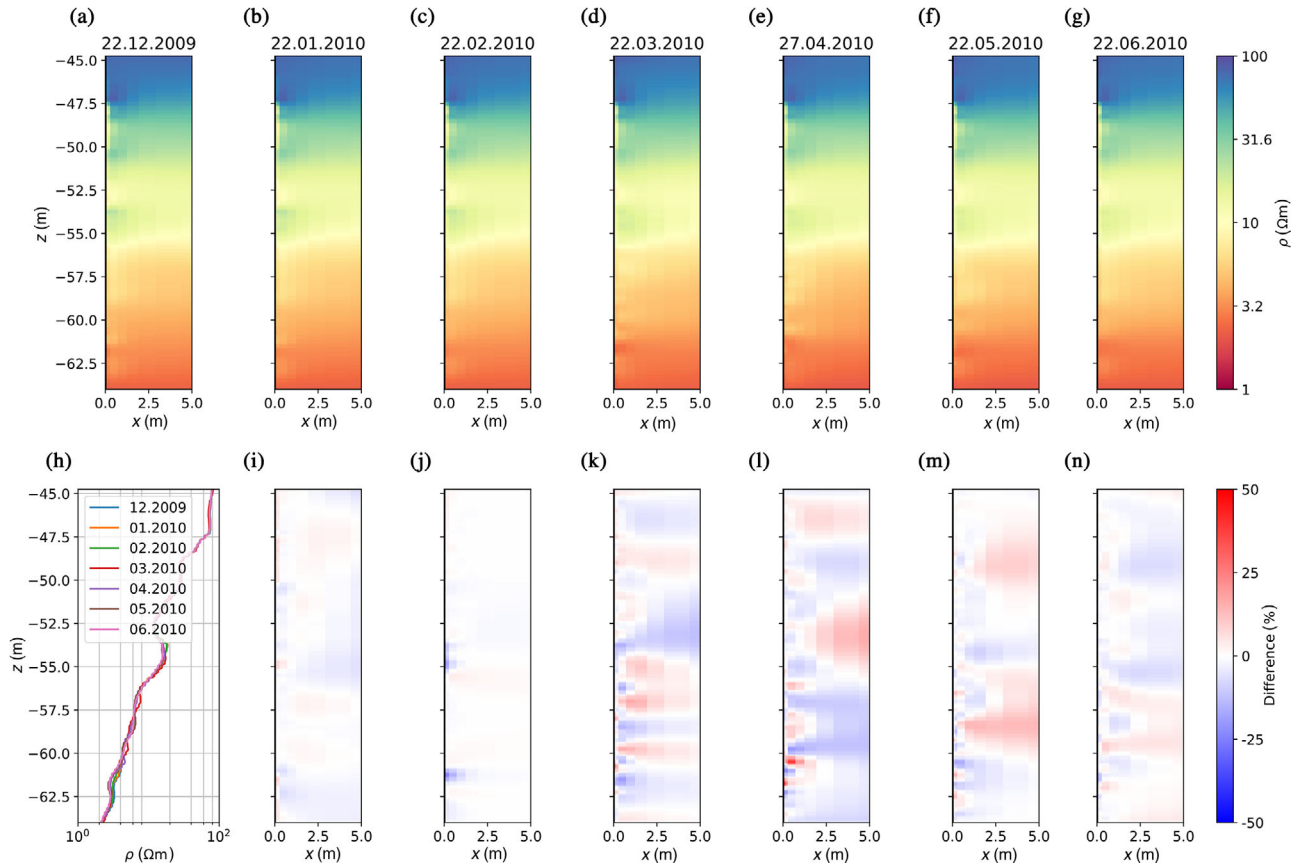
Figure 11 Dynamic inversion results of CLIWAT2 showing absolute resistivities (top) and relative differences from the previous time step. Resistivities at 1 m distance from the electrode chain are shown in (h) for all time steps.

inversion result cannot be interpreted easily, because different factors (pore water salinity and lithology, but also the drilling effects) are mixed up.

As the ρ_a is an integral value over a certain volume, the clay lenses affect the single four-point measurements to a certain extent. This changes as measurements progress, when the four-point array is shifted downwards to the next electrode. With increasing spacing, the ρ_a value averages a larger volume, which leads to smooth gradients between high- and low-resistivity parts for larger pseudo-levels. The more structural behaviour makes it difficult to determine a 10 Ωm interface in the pseudosection. In comparison, the inversion result on the right side in Fig. 8 shows resistivity variations within 1 m distance, which it makes it easier to find the 10 Ωm interface. The clay between 48.5 and 49.7 m and 52.4 and 52.8 m depths appears with smaller resistivities in the direct vicinity of SAMOS within 1 m distance. The third clay lens between 56 and 62.3 m depth cannot be resolved, because its resistivity is comparable to that of the saltwater-saturated sand.

The inverted section on the right-hand side shows a clearer image but is visually more structured compared to CLI-WAT1. We observe a smooth layering for more than 1 m distance. In general, we also see the transition zone from 100 Ωm at 47 m depth down to 3 Ωm at 60 m depth. However, it is influenced by both water salinity and lithology. For example, the clay layer at about 53 m depth is clearly visible with about 10 Ωm, as higher resistivity values appear below. In contrast, the clay layer at 49 m depth is harder to detect far from the borehole. A transition down to 3 Ωm appears within the deepest clay layer. Furthermore, the values in the sand below do not reach the expected values of approximately 2 Ωm, which indicate that the end of the transition zone has not been reached. Overall, the influence from the drilling seems lower. We only see lower resistivities around the two upper clay layers, which are probably due to the backfilled bentonite material.

Different from CLIWAT1 and CLIWAT2, the monitoring of goCAM1 records Wenner-α (WA) and dipole–dipole (DD)
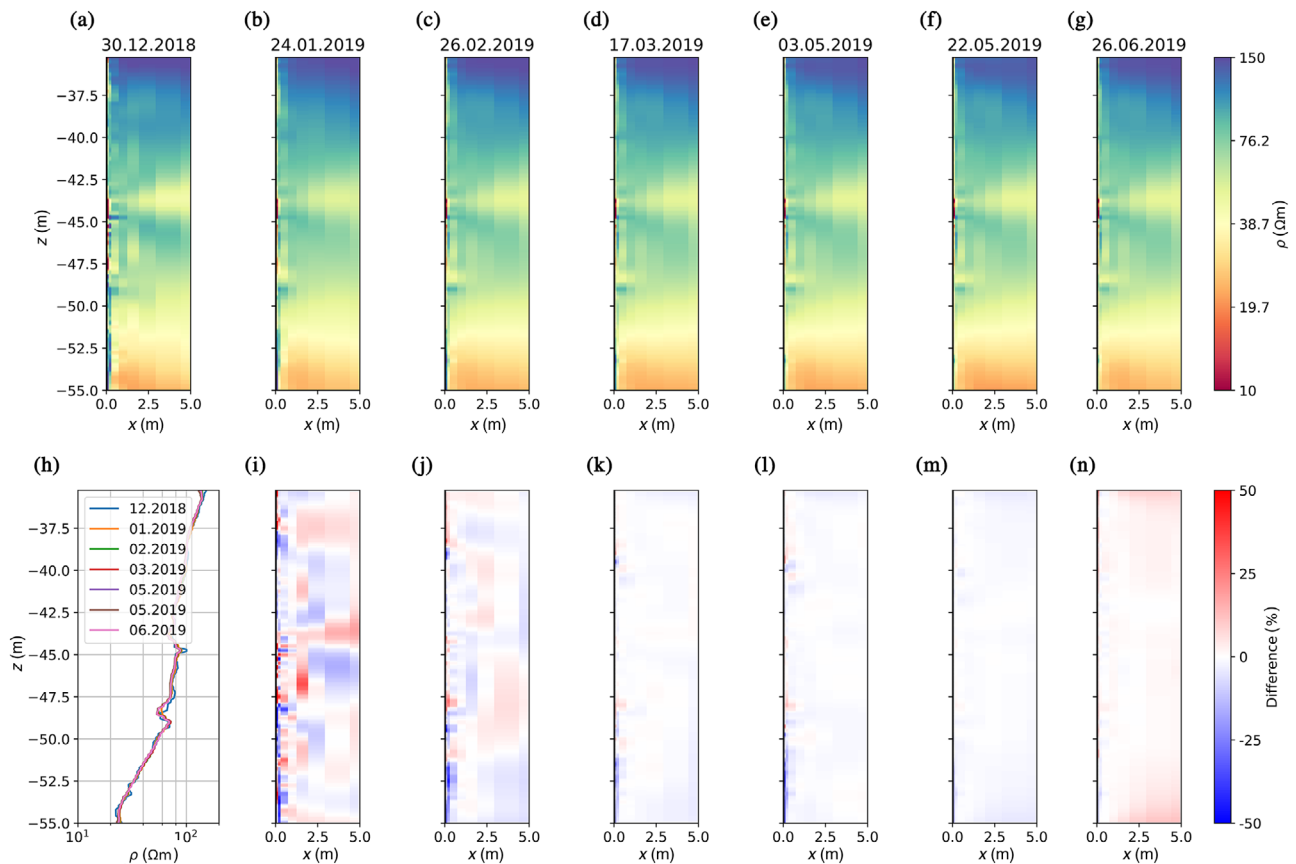
Figure 12 Dynamic inversion results of goCAM1, showing absolute resistivities (top) and relative differences from the previous time step. At resistivities in 1 m distance to the electrode chain are shown in (h) for all time steps.

arrays. The apparent resistivities, shown in Fig. 9 left, range from 10 to 240 Ωm, and thus they start with minimal ρ_a values that are ten times higher than those at the CLIWAT sites. Note that only 10 data points exceed 150 Ωm. Both arrays show a distinctive pattern at the lower clay interface at 44.8 m depth. As expected, the DD array can resolve structures along the electrode line much better that WA, because of its higher lateral resolution (which is, in this case, vertical).

The inversion result in Fig. 9 (right) shows a lot of resistivity changes along the z-direction and a zone with a higher resistivity level at 50 m depth and up to a distance of 0.3 m. Because the lithological log does not show geologic changes, the increased resistivities starting at $z = -50$ m indicate a higher-salinity zone. Two other low resistivity features appear at 48.5 m and 43 m depth, whose cause is not quite clear. As salinity should be increasing with depth, we can only suspect a higher silt or clay content. For the goCAM1 site, the resistivity distribution close to the boreholes is significantly different from the one adjacent to it. At the po-

sition of the clay layer, the filled bentonite clearly decreases the resistivity, whereas the higher values appear in the vicinity of the borehole at depths below 48 m. In contrast to the CLIWAT boreholes, there was no mud used during the drilling, which reduces the size of the affected zone. The backfilling material was flushed in a mixture with the freshwater, which in turn leads to higher resistivities. Note that the baseline measurement was made very shortly after the installation.

Dynamic inversion

The data shown were reduced to approximately one time step per month for all test sites. Larger or smaller gaps between the time steps occur, if the data files are corrupted beyond repair. The time-lapse inversion results of all three test sites show the resistivity distributions in the top row, along with the baseline result in subfigure (a), and the subsequent time steps in (b–g). The relative differences in percent from the previous

time step are shown in the bottom row (i–n). Resistivities along a vertical line at 1 m distance are shown in subfigure (h) for all shown time steps.

The resistivity distributions of the time-lapse results of CLIWAT1 (Fig. 10) show smooth models for later time steps (c–g), whereas the resistivities in Fig. 10 (a and b) are significantly reduced for $x \leq 1$ m. The difference plots for this model part ($x \leq 1$ m) show decreasing resistivities, which is most likely caused by remains of drilling mud in the backfilling that is slowly replaced by the formation fluid. It can also be seen that the resistivities increase again for $x \geq 1$ m. All other model parts show only small changes below 6% without a clear pattern that could be followed through the time steps. Note that resistivity changes below 57 m depth are smaller than 1 Ωm (Fig. 10h) for later time steps. The last time step in Fig. 10(g) has an overall shift to lower resistivities, but shows the same trend than all other models. The resistivity shift can be seen more clearly in Fig. 10(h). The difference between August 2010 and April 2010 shows that the resistivity values of the whole model from August are shifted and not just in some parts. This can also be seen in all subsequent time steps after August 2010 (not shown here). As the apparent resistivities also show the shift, it is most likely not an inversion artefact. The decreased resistivity could be explained by an increased pumping rate that occurs every year during the summer season, because of the enormous amount of tourists visiting the island.

The time-lapse results of CLIWAT2 in Fig. 11 show, similar to CLIWAT1, small resistivity changes with the exception of the first difference plot. A clear pattern can be recognized, showing an increasing resistivity in the upper model part lying above 48 m depth, a decreasing resistivity for model parts deeper than 60 m and vice versa in between (48–60 m depth). However, the approximately 6 m thick clay layer, between 56 and 62.7 m depths, should show very low or no variations, which is not the case as Fig. 11(i–n). Keeping the geological conditions in mind (see Fig. 6), we expect no or little variations within the clay layer (should be clearest for the deepest one). The region at 54 m depth, that corresponds to the sand between the second and the third clay layers, shows decreasing resistivities for the first time steps, which appears to decrease weaker in April and May. Absolute resistivity changes at 1 m distance from SAMOS (Fig. 11h) are less than 4 Ωm for depths below 55 m. However, all resistivity lines in Fig. 11(h) show only very little variation between each other, except for the first time step.

The results of goCAM1 in Fig. 12 show that the largest resistivity variations appear between the first and the second time step (like CLIWAT2) and that the differences between the subsequent time steps are almost gone after February 2019, that is 3 months after the installation. Figure 12(a) shows that the resistivity values and changes along the z-direction are most significant, which cause stronger compensation of artefacts to distances up to 2 m. A more continuous resistivity trend appears in Fig. 12(b) with significantly reduced artefacts, which are vanished after 3 months. Although the difference plot shows large changes, the resistivity distributions in Fig. 12(a–g) show that the effect due to the drilling vanishes similarly fast. However, the baseline and the vertical resistivity lines of all time steps in Fig. 12(h) proves that the resistivity trend can be reconstructed quite accurately at 1 m distance. The resistivity changes that occur are most likely caused by changes of the backfilling material; otherwise the overall resistivity variation is in a quite stable state.

CONCLUSIONS

We have presented a methodology for analysing the monitoring data from vertical electrode chains to observe freshwater–saltwater interfaces and their dynamics. The numerical framework accurately models the whole geometry of the tool including the finite electrodes, using the complete electrode model. For inversion, we reduce the inherently three-dimensional (3D) problem to two dimensions by using a region technique. This constraint was made, because a 2D electrode setup cannot resolve a 3D resistivity distribution correctly. As a result, we are able to differentiate anomalies close to the borehole from the undisturbed subsurface.

Data from three different installed systems were analysed both statically and dynamically. The CLIWAT1 borehole, exhibiting a very simple sandy geology, shows a smooth transition zone located between fresh and saline water. In contrast, for CLIWAT2, where clayey and sandy layers are interbedded, the results are affected by both geology and fluid salinity - that are difficult to differentiate from each other without additional information. The third case, goCAM1, shows the largest differences between the near-borehole region and the undisturbed case, mostly attributed to the backfilling of the installation process. A comparison with the lithological log shows some inconsistencies, that could hint to deviations from the one-dimensional case.

We have analysed the temporal changes in the subsurface for a period of some months since the installation, using a time-lapse inversion approach. Most changes occur directly after the installation in the vicinity of the boreholes and they are caused by the adaption towards the undisturbed case, for

example by the saturation of the backfilling with the formation fluid. Changes at larger distances from the boreholes are much smaller and they represent a more reliable description of the ongoing processes of the freshwater–saltwater interaction in the course of the hydrological boundary conditions, for example pumping or recharge. The goCAM1 case shows that a combination of different electrode arrays is favourable in order tio achive a good resolution. In order to verify the plausibility of the observed dynamics, longer monitoring periods are required. Groundwater modelling could be helpful to interpret the changes from a hydraulic perspective.

ACKNOWLEDGEMENTS

DATA AVAILABILITY STATEMENT

The data sets used for this article are openly available (Ronczka *et al*., 2020) under http://doi.org/10.5281/ZENODO.3609110.

ORCID

Mathias Ronczka 🔟
https://orcid.org/0000-0001-6044-1762

REFERENCES

Baisset, M. and Neyens, D. (2018) High frequency saltwater intrusion monitoring using borehole geophysical tools (SMD). In: *25th Salt Water Intrusion Meeting*, 17–22 June 2018, Gdansk, Poland.

Binley, A., Winship, P., West, L., Pokar, M. and Middleton, R. (2002) Seasonal variation of moisture content in unsaturated sandstone inferred from borehole radar and resistivity profiles. *Journal of Hydrology*, 267, 160–172.

Cheng, A.-D., Halhal, D., Naji, A. and Ouazar, D. (2000) Pumping optimization in saltwater-intruded coastal aquifers. *Water Resources Research*, 36, 2155–2165.

Cooper, H. (1959) A hypothesis concerning the dynamic balance of fresh water and salt water in a coastal aquifer. *Journal of Geophysical Research*, 64, 461–467.

Coscia, I., Greenhalgh, S., Linde, N., Doetsch, J., Marescot, L., Günther, T. and Green, A. (2011) 3D crosshole apparent resistivity static inversion and monitoring of a coupled river-aquifer system. *Geophysics*, 76, G49–59.

Doetsch, J., Coscia, I., Greenhalgh, S., Linde, N., Green, A. and Günther, T. (2010) The borehole-fluid effect in electrical resistivity imaging. *Geophysics*, 75(4), F107–F114.

Ferguson, G. and Gleeson, T. (2012) Vulnerability of coastal aquifers to groundwater use and climate change. *Nature Climate Change*, 2, 342–345.

Grinat, M., Südekum, W., Epping, D., Grelle, T. and Meyer, R. (2010) An automated electrical resistivity tomography system to monitor the freshwater/saltwater zone on a north sea island. In: *Near Surface 2010–16th EAGE European Meeting of Environmental and Engineering Geophysics*. EAGE Publications. https://doi.org/10.3997/2214-4609.20144785.

Günther, T. and Müller-Petke, M. (2012) Hydraulic properties at the North Sea island of Borkum derived from joint inversion of magnetic resonance and electrical resistivity soundings. *Hydrology and Earth System Sciences*, 16(9), 3279–3291.

Igel, J., Günther, T. and Kuntzer, M. (2013) Ground-penetrating radar insight into a coastal aquifer: the freshwater lens of Borkum Island. *Hydrology and Earth System Sciences*, 17, 519–531.

Kemna, A., Vanderborght, J., Kulessa, B. and Vereecken, H. (2002) Imaging and characterisation of subsurface solute transport using electrical resistivity tomography (ERT) and equivalent transport models. *Journal of Hydrology*, 267, 125–146.

Kuras, O., Pritchard, J., Meldrum, P.I., Chambers, J.E., Wilkinson, P.B., Ogilvy, R.D. and Wealthall, G.P. (2009) Monitoring hydraulic processes with automated time-lapse electrical resistivity tomography (ALERT). *Compte Rendus Geosciences – Special Issue on Hydrogeophysics*, 341, 868–885.

Loke, M.H., Chambers, J.E., Rucker, D.F., Kuras, O. and Wilkinson, P.B. (2013) Recent developments in the direct-current geoelectrical imaging method. *Journal of Applied Geophysics*, 95, 135–156.

Ogilvy, R.D., Meldrum, P.I., Kuras, O., Wilkinson, P.B., Chambers, J.E., Sen, M., Pulido-Bosch, A., Gisbert, J., Jorreto, S., Frances, I. and Tsourlos, P. (2009) Automated monitoring of coastal aquifers with electrical resistivity tomography. *Near Surface Geophysics*, 7, 367–375.

Rasmussen, P., Sonnenborg, T.O., Goncear, G. and Hinsby, K. (2013) Assessing impacts of climate change, sea level rise, and drainage canals on saltwater intrusion to coastal aquifer. *Hydrology and Earth System Sciences*, 17, 421–443.

Ronczka, M., Günther, T. and Grinat, M. (2020) SAMOS monitoring data for CLIWAT1, CLIWAT2 and goCAM1. https://doi.org/10.5281/zenodo.3609110.

Ronczka, M., Rücker, C. and Günther, T. (2015) Numerical study of long-electrode electric resistivity tomography — Accuracy, sensitivity, and resolution. *Geophysics*, 80, E317–E328.

Rücker, C. and Günther, T. (2011) The simulation of finite ert electrodes using the complete electrode model. *Geophysics*, 76, F227–F238.

Rücker, C., Günther, T. and Wagner, F.M. (2017) pyGIMLi: An open-source library for modelling and inversion in geophysics. *Computers and Geosciences*, 109, 106–123.

Rucker, D.F., Loke, M.H., Levitt, M.T. and Noonan, G.E. (2010) Electrical-resistivity characterization of an industrial site using long electrodes. *Geophysics*, 75, WA95–WA104.

Schneider, J.C. and Kruse, S.E. (2006) Assessing selected natural and anthropogenic impacts on freshwater lens morphology on small barrier islands: Dog Island and St. George Island, Florida, USA. *Hydrogeology Journal*, 14, 131–145.

Schöniger, H., Eley, M., Langman, T., Schimmelpfenning, S., Kejo, H., Sander, M., Wiederhold, H., Ronczka, M., Schneider, A., Zhao, H. and Koch, A. (2019) Salt water meets fresh water - scientific approach meets social needs. In: *Proceedings of the 38th IAHR World Congress*, Panama City, Panama.

Sherif, M., Kacimov, A., Javadi, A. and Ebraheem, A.A. (2012) Modeling groundwater flow and seawater intrusion in the coastal aquifer of Wadi Ham, UAE. *Water Resources Management*, 26, 751–774.

Si, H. (2015) Tetgen, a delaunay-based tetrahedral mesh generator. *ACM Transactions on Mathematical Software*, 41, 1–36.

Siemon, B., Costabel, S., Voß, W., Meyer, U., Deus, N., Elbracht, J., Günther, T. and Wiederhold, H. (2015) Airborne and ground geophysical mapping of coastal clays in Eastern Friesland, Germany. *Geophysics*, 80, WB21–WB34.

Siemon, B., Steuer, A. and Meyer, U. (2018) Review of BGR's HEM surveys in Germany. In: *Proceedings of 7th International Workshop on Airborne Electromagnetics*, Kolding, DK.

Sulzbacher, H., Wiederhold, H., Siemon, B., Grinat, M., Igel, J., Burschil, T., Günther, T. and Hinsby, K. (2012) Numerical mod-
elling of climate change impacts on freshwater lenses on the North Sea island of Borkum using hydrological and geophysical methods. *Hydrology and Earth System Sciences*, 16, 3621–3643.

Tsourlos, P., Ogilvy, R., Meldrum, P. and Williams, G. (2003) Time-lapse monitoring in single boreholes using electrical resistivity tomography. *Journal of Environmental and Engineering Geophysics*, 8, 1–14.

Tsourlos, P., Vargemezis, G., Voudouris, C., Spachos, T. and Stampolidis, A. (2007) Monitoring recycled water injection into a confined aquifer in Sindos (Thessaloniki) using electrical resistivity tomography (ERT): installation and preliminary results. *Bulletin of the Geological Society of Greece*, 40, 580.

Watlet, A., Kaufmann, O., Triantafyllou, A., Poulain, A., Chambers, J.E., Meldrum, P.I., Wilkinson, P.B., Hallet, V., Quinif, Y., Van Ruymbeke, M., and Van Camp, M. (2018) Imaging groundwater infiltration dynamics in the karst vadose zone with long-term ERT monitoring. *Hydrology and Earth System Sciences*, 22, 1563–1592.

Whiteley, J.S., Chambers, J.E., Uhlemann, S., Wilkinson, P.B. and Kendall, J.M. (2019) Geophysical monitoring of moisture-induced landslides. *A Review: Reviews of Geophysics*, 57, 106–145.

Wiederhold, H., Sulzbacher, H., Grinat, M., Günther, T., Igel, J., Burschil, T. and Siemon, B. (2013) Hydrogeophysical characterization of freshwater/saltwater systems – case study, Borkum Island, Germany. *First Break*, 31, 109–117.